Assessment of dosimetric impact of system specific geometric distortion in an MRI only based radiotherapy workflow for prostate

Gustafsson, C; Nordström, F; Persson, E; Brynolfsson, J; Olsson, L E

Published in:
Physics in Medicine and Biology

DOI:
10.1088/1361-6560/aa5fa2

2017

Document Version:
Peer reviewed version (aka post-print)

Assessment of dosimetric impact of system specific geometric distortion in an MRI only based radiotherapy workflow for prostate

C GUSTAFSSON[1,2], F NORDSTRÖM[3], E PERSSON[1], J BRYNOLFSSON[4] and L E OLSSON[2]

1) Department of Hematology, Oncology and Radiation Physics, Skåne University Hospital, Lund Sweden

2) Department of Medical Physics, Lund University, Malmö, Sweden

3) Department of Medical Physics and Biomedical Engineering, Sahlgrenska University Hospital, Gothenburg, Sweden

4) Spectronic Medical AB, Helsingborg, Sweden

E-mail: christian.k.gustafsson@skane.se

Abstract

Dosimetric errors in a magnetic resonance imaging (MRI) only radiotherapy workflow may be caused by system specific geometric distortion from MRI. The aim of this study was to evaluate the impact on planned dose distribution and delineated structures for prostate patients, originating from this distortion. A method was developed, in which computer tomography (CT) images were distorted using the MRI distortion field.

The displacement map for an optimized MRI treatment planning sequence was measured using a dedicated phantom in a 3T MRI system.

To simulate the distortion aspects of a synthetic CT (electron density derived from MR images), the displacement map was applied to CT images, referred to as distorted CT images. A volumetric modulated arc prostate treatment plan was applied to the original CT and the distorted CT, creating a reference and a distorted CT dose distribution.

By applying the inverse of the displacement map to the distorted CT dose distribution, a dose distribution in the same geometry as the original CT images was created. For 10 prostate cancer patients, the dose difference between the reference dose distribution and inverse distorted CT dose distribution was analyzed in isodose level bins.

The mean magnitude of the geometric distortion was 1.97 mm for the radial distance of 200-250 mm from isocenter. The mean percentage dose differences for all isodose level bins, were ≤ 0.02 % and the radiotherapy structure mean volume deviations were < 0.2 %.

The method developed can quantify the dosimetric effects of MRI system specific distortion in a prostate MRI only radiotherapy workflow, separated from dosimetric effects originating from synthetic CT generation. No clinically relevant dose difference or structure deformation was found when 3D distortion correction and high acquisition bandwidth was used. The method could be used for any MRI sequence together with any anatomy of interest.

1. Introduction

The use of dedicated magnetic resonance imaging (MRI) scanners in radiotherapy centers has rapidly increased due to the superior soft tissue contrast of the MRI compared to computer tomography (CT) (Karlsson et al., 2009, Blomqvist et al., 2013). For external radiotherapy of prostate cancer, MRI can add clinical value to the target delineation process (Debois et al., 1999, Jackson et al., 2007). Simultaneous use of multimodal image information from CT and MRI often requires a registration of the images into a common frame of reference. This multimodal image registration between CT and MRI can result in an increased spatial uncertainty and therefore result in a deviation of the planned dose to the patient (Nyholm et al., 2009)**.** To avoid these uncertainties, techniques to provide electron density information from MRI have been developed, enabling a workflow excluding the CT. These workflows are often referred to as MRI only workflows where a synthetic CT image, created from MRI, replaces the CT. Several techniques to generate synthetic CTs has been proposed (Lambert et al., 2011, Dowling et al., 2012, Johansson et al., 2012, Hsu et al., 2013, Edmund et al., 2014, Korhonen et al., 2014, Andreasen et al., 2015, Siversson et al., 2015). The time, effort and resources spent per patient can also be reduced by excluding the CT from the radiotherapy workflow. This would also be beneficial as no ionizing radiation is used during radiotherapy planning.

The generation of a synthetic CT requires a field of view (FOV) covering the outer body contour for accurate treatment planning. Magnetic resonance (MR) images solely used for organ at risk (OAR)- and target delineation, does not require coverage of the outer body contour. These MR images are often acquired with a smaller FOV and used in conjunction with CT.

Geometric accuracy in the images used for radiotherapy treatment planning and positioning is essential and CT is considered as the gold standard in this context. Geometric distortion are known to exist in MRI and concerns regarding the use of MRI in radiotherapy has therefore been raised (Weygand et al., 2016). The geometric distortion from MRI can be divided into system specific or patient/object specific distortion. The system specific distortion can originate from the non-linear gradients or from the non-homogenous static magnetic field (Bakker et al., 1992, Doran et al., 2005, Reinsberg et al., 2005). The

patient/object specific distortion can originate from magnetic susceptibility or from chemical shift effects (Bellon et al., 1986, Bakker et al., 1992).

The size of the geometric distortion originating from the non-linear gradients is increasing with increasing distance from the MRI magnetic isocenter (Wang et al., 2004b, Walker et al., 2014) and is therefore highly dependent on the size of the FOV used in the MRI acquisition.

It has been shown that the system specific geometric distortion are larger than the patient specific geometric distortion (Wang et al., 2004b) and that non-linear gradients are the main source of geometric distortion (Baldwin et al., 2007). The system specific geometric distortion in terms of non-linear gradients can in modern MR scanners be corrected in 2 dimensions (2D) using MRI vendor specific software (Wang et al., 2004b). The availability of 3D correction of the non-linear gradients can be dependent on the acquisition sequence and acquisition parameters (Walker et al., 2015). The system- and patient/object specific geometric distortion, in terms of induced non-homogeneities in the magnetic field, can be mitigated by the use of active magnetic field shimming (Weygand et al., 2016).

Several methods have been proposed for measuring and mapping the system specific geometric distortion using dedicated phantoms (Koch et al., 2003, Wang et al., 2004a, Torfeh et al., 2015). These phantoms often have some kind of visual signal markers at known spatial positions. To assess the geometric distortion, the marker positions in the MR images is compared with the physical location of the markers. Due to the need of large volume coverage special phantoms have been designed for that purpose (Tadic et al., 2014, Torfeh et al., 2015, Walker et al., 2015, Huang et al., 2016).

A geometric distortion of < 2 mm in the anatomy of interest is desired for the use of MRI in radiotherapy (Walker et al., 2015, Weygand et al., 2016). It was previously shown that residual geometric distortion, measured for a clinically relevant acquisition sequence together with 3D correction, were > 2 mm at distances > 15 cm from the isocenter (Walker et al., 2015). It was also concluded that the origin of the geometric distortion were dominated by effects from non-linear gradients.

It is of broad and immediate interest to study the dosimetric effects from system specific geometric distortion in an MRI only radiotherapy workflow for prostate. Attempts has earlier been made to

quantify how the geometric error in MRI propagates through the MRI only radiotherapy treatment planning process and how it affects the planned dose distribution (Mah et al., 2002, Petersch et al., 2004, Sun et al., 2015).

The combined dosimetric impact from the system specific geometric distortion and a synthetic CT generation method was recently investigated (Bolard and Bulling, 2016). Dosimetric errors originating from multiple previously published synthetic CT generation methods has also been studied (Kim et al., 2015). In the clinical introduction of an MRI only radiotherapy treatment planning workflow it is important to solely quantify the dosimetric errors from geometric distortion. The methodology presented in this work enables separation of the dosimetric errors introduced by the system specific geometric distortion from the dosimetric errors originating from the synthetic CT generation itself.

The aim of this study was to 1) develop a method for MRI quality control and validation of clinical MRI sequences for the use in an MRI only radiotherapy workflow. 2) Evaluate the magnitude of the system specific geometric distortion in an MRI system and the impact on delineated structures. 3) Evaluate, using the developed method, the dosimetric impact of the system specific geometric distortion. This was done using a clinical MRI acquisition sequence, designed for an MRI only prostate radiotherapy workflow. We propose a methodology to apply the geometric distortion, originating from system related distortion in MRI, on pre-existing patient CT images.

2. Methods

The study was divided into three parts where the first part covered the measurement of geometric distortion in MRI, the generation of the displacement map and its application. The second part investigated the impact of geometric distortion on delineated radiotherapy structures (RT structures). The final part investigated the dosimetric impact of geometric distortion in MRI only treatment planning. The workflow of the method, illustrated in figure 2, was repeated for 10 prostate cancer patients (median age 75 years, median weight 84 kg and median length 173 cm), consecutive chosen from an ongoing in-vivo MRI only treatment planning study.

2.1 Data acquisition, displacement map generation and its application

A commercially available 3D phantom designed to assess geometric accuracy for large FOVs (Spectronic Medical AB, Helsingborg, Sweden) was used in this study. The phantom contained 1177 spherical markers, with a marker diameter of 17 mm, filled with polyethylene glycol. The markers were organized in a grid on layers of extruded polystyrene which covered 438.7 x 346.0 x 470.0 mm^3 (width (W), height (H), length (L)). The outer case of the phantom covered 502 x 404 x 534 mm^3 (W, H, L) and was built by a layer of polyvinyl chloride (PVC), with a thickness of 1 mm around the phantom and 10 mm at the sides. Total weight of the phantom was 9.8 kg. A 3T wide bore 70 cm MRI system (Discovery 750W, Software DV25R02-1549b, General Electric Healthcare, Milwaukee, WI) was selected for investigation. The phantom was scanned using the built in 2 channel body RF- multi transmit and receive coil (figure 1). The patient CT images used in this study were acquired with a Siemens Somatom Definition AS+ (Siemens Healthcare, Forchheim, Germany), slice thickness 3 mm, reconstructed diameter 500 mm, reconstructed in plane resolution 0.98 mm x 0.98 mm, peak kilo voltage output 120 kV, exposure time 500 ms, tube current 291 mA-677 mA.

Figure 1. The commercially available phantom from Spectronic Medical AB is designed to assess geometric accuracy. It was placed on the MRI table without table top. Lines on the phantom surface was used to align the phantom using the built in laser positioning system on the MRI.

For accurate and comparable mapping of the geometric distortion, arising principally from system specific geometric distortion, it was of importance that an identical MRI sequence was used for the phantom and the in-vivo MRI only treatment planning study. The parameters used in the phantom MRI acquisition sequence were copied from the in-vivo MRI acquisition sequence used in an ongoing Swedish multi-center study (MR-Only Prostate External Radiotherapy, MR-OPERA). Due to the phantom size, the FOV and number of slices had to be adjusted. The in-vivo study was performed with MRI acquisition sequence parameters described in table 1. The acquisition sequence for the phantom was considered and referred to as the optimized acquisition sequence.

The phantom was placed above the superior cavity on the MRI patient table, no table top was used (figure 1). The phantom was scanned with the optimized acquisition sequence. The displacement map was calculated using a cloud based commercial analysis software, GRADE version 1.0.32 (Spectronic Medical AB, Helsingborg, Sweden). GRADE automatically calculated the locations of the phantom markers in the MR images using a non-rigid image registration with a digital reference model of the phantom. Reference markers from the digital reference phantom model were generated by a rigid

registration between the digital reference phantom model and the MR images using only the markers close to the isocenter, where geometric distortion were considered to be negligible. For each marker, the difference in location between the reference marker in the rigidly registered digital reference phantom model and the marker in the MR images were calculated. The displacement map, describing the difference in the location of the markers, were calculated using inverse mapping (Beier and Neely, 1992) and generated with the pixel dimensions 0.875 mm x 0.875 mm x 0.8741 mm. A binary mask was applied to the displacement map to exclude peripheral sub-volumes with non-reliable displacement data.

Using an in-house built MATLAB software version R2015a (Mathworks Inc., Sherborn, MA, USA), the displacement map were linearly interpolated (down sampled) to match the pixel dimensions of the CT images. The magnitude of the geometric distortion for separate spatial directions were derived from, and equal to, the data from the displacement map. The relative orientation of the displacement map in space with respect to the CT images was taken into account before applying the displacement map to the CT. This was performed by a translation of the left-right and inferior-superior center of the displacement map to the DICOM user defined origin in the CT images **(**determined by the position of external skin markers, applied to the patient before CT scanning). A translation of the anterior-posterior center of the displacement map positioned the posterior anatomy of the CT images in the corresponding MRI geometry.

To simulate a clinical scan situation, and to avoid the use of unreliable displacement data originating from a peripheral part of the phantom, the displacement map was limited to 30 cm in the inferior-superior direction before being applied to the CT images. CT data outside of the 30 cm inferior-superior coverage was left undistorted. The displacement map was applied to the CT images as a geometric transformation using linear interpolation, from here on referred to as distCT images (figure 2).

To estimate the possible impact of object specific geometric distortion an additional MRI scan was performed on the phantom. The magnitude of the object specific geometric distortion in the optimized acquisition sequence was assumed to be proportional to the magnitude of the deviations in the static magnetic field and inversely proportional to the read out gradient strength (Weygand et al., 2016). The deviations in the magnetic field, induced by the magnetic susceptibility of the phantom, was measured

using the sequence IDEAL IQ (General Electric Healthcare, Milwaukee, WI), acquisition sequence parameters described in table 1. The clinical purpose of IDEAL IQ is in-vivo fat quantification and depends on a correct assessment of the deviations in the static magnetic field, i.e. field mapping. The phantom volume field map was exported and the magnitude of the object specific geometric distortion was calculated given a read out gradient strength of 13.1 mTesla/m (used in the optimized acquisition sequence).

Table 1. MRI acquisition sequence parameters for the acquisition sequences referred to in this study. The in-vivo MRI acquisition sequence was used in an ongoing Swedish multi-center study (MR-Only Prostate External Radiotherapy, MR-OPERA). The optimized acquisition sequence was used to scan the phantom to acquire the displacement map. The IDEAL IQ sequence was used to estimate the possible impact of object specific geometric distortion.

Parameter	In-vivo study	Optimized acquisition sequence	IDEAL IQ
Coil	GE GEM Anterior Array	Built-in Body	Built-in Body
Sequence type	FSE [a]	FSE [a]	GRE
2D/3D	2D	2D	3D
Scan Plane	Axial	Axial	Axial
Freq. FOV	448 mm [b]	448 mm [b]	500 mm [b]
Phase FOV	314 mm [c]	403 mm [c]	500 mm
Scan matrix (Freq. x phase)	640 x 512	640 x 512	160 x 160
Recon. matrix (Freq. x phase)	1024 x 1024	1024 x 1024	256 x 256
TR	15000.0 ms	15000.0 ms	6.0 ms
TE	96 ms	96 ms	0.89, 1.63, 2.36, 3.10, 3.83, 4.56 ms
Slice thickness	2.5 mm	2.5 mm	6.0 mm
Slice spacing	0.0 mm	0.0 mm	0.0 mm
Number of slices	88	200	100
Number of echoes	1	1	6
3D geometry correction	On	On	Off
Bandwidth / pixel	390 Hz	390 Hz	1389 Hz
Shimming method	Auto (first order)	Auto (first order)	Auto (first order)
RF transmit mode	Multi transmit	Multi transmit	Quadrature
Acquisition time	7 minutes	24 minutes	6.5 minutes

[a] Sequence used was Fast Recovery Fast Spin Echo (FRFSE)
[b] Right-Left direction
[c] Anterior-Posterior direction

2.2 Impact on RT structures

To assess the possible geometric distortion for target- and OAR anatomy, the impact on the delineated RT structures in the CT images was investigated. This was done using an in-house developed MATLAB software. By using the phantom marker locations from the detected markers in the MR images and the reference marker locations, supplied by Spectronic Medical AB and described in section 2.1, the displacement was calculated for all points in the RT structures. The relative orientation of the displacement data in space with respect to the RT structure was taken into account before calculating

the displacement to the RT structure points, using the same orientation adaptations as described in section 2.1. The displacement was applied to the RT structure points using linear interpolation.

The external surface of the RT structures were defined using additional RT structure points inserted in the areas encompassed by the first and last slice of the RT structure volume. A 3D boundary and its convex hull was calculated from the external surface, and the ratio of the volume within the 3D convex hull for distorted and original RT structures was calculated. In an absence of volume deviation, between original and distorted RT structure, a uniform translation and/or deformation with constant volume, of the whole RT structure could exist. This could give rise to deviation in the RT structure but no deviation in RT structure volume. To be able to detect such an event, the magnitude of the distortion in each spatial direction were calculated for each RT structure.

2.3 Treatment planning and dosimetric analysis

The RT structures for target and OAR were copied from the original CT to the distCT images. The RT structures were not deformed prior to copying them as the only objective was to enable the calculation of an acceptable treatment plan. A single arc 10 MV VMAT prostate treatment plan (78 Gy/39 fractions) were optimized on the distCT images using the Eclipse Treatment Planning system version 13.6 (Varian Medical Systems, Palo Alto, USA). The final dose distribution, referred to as D_{distCT}, was calculated using the Analytical Anisotropic Algorithm. The treatment plan was confirmed to fulfill the dose criterions in the conventional arm of the Swedish multicenter Phase III study of HYPO-fractionated Radiotherapy of intermediate risk localized Prostate Cancer (Widmark, 2008). The created treatment plan was applied and recalculated with identical field setup and number of monitor units on the original CT images, creating a reference dose distribution D_{refCT}. This was performed in order to exclude any difference due to a slightly different plan delivery. Workflow is illustrated in figure 2. The dose distributions D_{distCT} and D_{refCT} were linearly interpolated to match the pixel dimensions of the CT images.

The percentage dose difference between D_{distCT} and D_{refCT} was not calculated directly, since the distCT was considered geometrically incorrect. In an MRI only workflow, the dose distribution calculated on a synthetic CT (resembled by the distCT) is the dose distribution that would have been used for treatment. By applying the inverse of the displacement map to the D_{distCT} the planned dose distribution was

transferred into a geometrically correct frame of reference which easily could be compared to the dose distribution of the original CT (D_{refCT}), considered the gold standard. The inversely deformed dose distribution was referred to as D_{distCT_inv}. This is in analogy with the process of adaptive radiotherapy in a conventional CT based workflow using deformable image registration and dose warping (Veiga et al., 2015).

The inverse of the displacement map (not to be confused with inverse mapping) was iteratively calculated using the function InvertDisplacementFieldImageFilter in Simple ITK 0.9.0 (open-source) together with ITK 4.7.2 (Yoo et al., 2002). To verify the existence of an inverse to the displacement map and detect possible noninvertible displacement data, the value and the sign of the determinant of the displacement map Jacobian was evaluated for all patients. The value of zero corresponds to a nonexistent inverse and negative values are indicative of noninvertible and unrealistic deformations (Chen et al., 2008, Veiga et al., 2015). The inverse of the displacement map was applied using nearest neighbor interpolation in an in-house developed MATLAB software.

The percentage dose difference (normalized to 78 Gy), referred to as ΔD, was calculated in the interval 0 % to 100 % by subtracting D_{refCT} and D_{distCT_inv} in segmented binned isodose levels with a binning of 5 %. The segmentations were determined from the D_{refCT} using binary masks. The mean and the standard deviation of the segmented ΔD was calculated for each binary mask, i.e. for each binned isodose level, for each patient. The binning method was performed rather than using intentionally distorted RT structures or re-delineated RT structures in the distCT. A manual re-delineation in the distCT images would give rise to additional uncertainties as a result. The workflow is illustrated in figure 2.

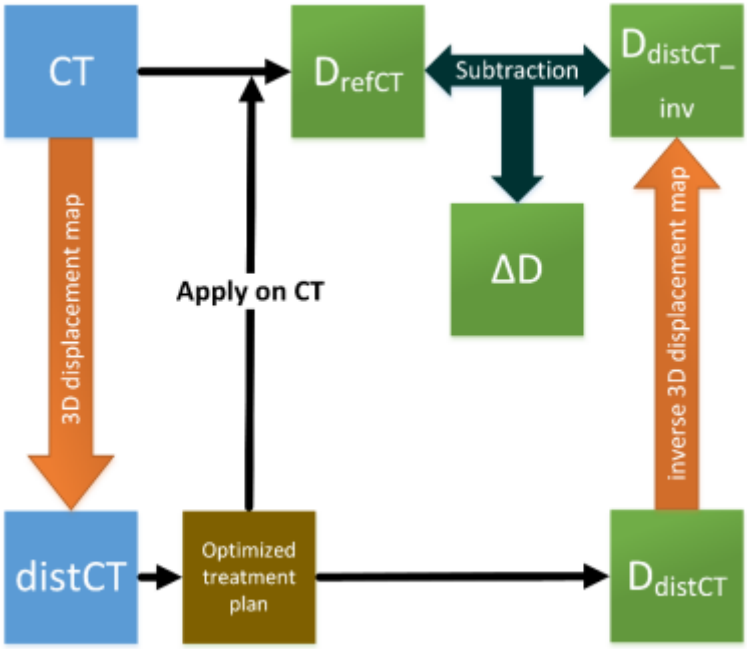

Figure 2. Flow chart of operations on CT images and dose distributions. **CT** = original CT images, **distCT** = distorted CT images, $\mathbf{D}_{\mathbf{distCT}}$ = dose distribution from **distCT**, $\mathbf{D}_{\mathbf{refCT}}$ = dose distribution from **CT**, $\mathbf{D}_{\mathbf{distCT\_inv}}$ = dose distribution from **distCT** with the inverse of the displacement map applied, $\Delta\mathbf{D}$ = dose difference $\mathbf{D}_{\mathbf{refCT}} - \mathbf{D}_{\mathbf{distCT\_inv}}$.

3. Results

3.1 Geometric distortion measurements

The mean, minimum and maximum magnitude of the phantom geometric distortion in separate spatial directions, for complete and limited phantom volumes is presented in table 2. The mean magnitude for the geometric distortion was largest for the inferior-superior direction. This behavior was true in both the limited (30 cm inferior-superior) and the complete phantom volume. The mean and maximum magnitude of the phantom geometric distortion as a function of radial distance from the isocenter of the MRI, is presented for the complete phantom volume in table 3. The mean and maximum magnitude of the deviations in the static magnetic field, together with the calculated magnitude of the object specific geometric distortion for the complete phantom volume, is displayed in table 4.

Table 2. Mean, minimum (min) and maximum (max) magnitude of the phantom geometric distortion for separate spatial directions, for complete and limited (30 cm inferior-superior) phantom volumes. Data was binary masked for both phantom volumes to exclude peripheral sub-volumes with non-reliable displacement data. Data was not interpolated to match the pixel dimensions of the CT images.

	Left-Right (mm)			Anterior-Posterior (mm)			Inferior-Superior (mm)		
	Mean	Min	Max	Mean	Min	Max	Mean	Min	Max
Limited phantom volume	0.082±0.19	0.00	3.60	0.070±0.16	0.00	3.51	0.36±0.76	0.00	9.67
Complete phantom volume	0.13±0.37	0.00	12.28	0.10±0.33	0.00	12.58	0.47±0.96	0.00	9.67

Table 3. Mean and maximum magnitude of the phantom geometric distortion, complete phantom volume, as a function of radial distance from the isocenter of the MRI. Data was binary masked to exclude peripheral sub-volumes with non-reliable displacement data. Data was not interpolated to match the pixel dimensions of the CT images.

Radial distance from isocenter and distortion (mm)							
< 100		100-150		150-200		200-250	
Mean	Max	Mean	Max	Mean	Max	Mean	Max
0.17	0.43	0.3	0.82	0.57	1.85	1.97	7.86

Table 4. Mean and maximum magnitude of deviations in the magnetic field (ppm) for the phantom volume, as a function of radial distance from the isocenter of the MRI, measured with the IDEAL IQ sequence. The calculated magnitude of the object specific geometric distortion for the phantom using the optimized sequence is displayed in parenthesis.

Measured deviation of the magnetic field (ppm) and calculated distortion (mm) at different radial distances from isocenter (mm)							
< 100		100-150		150-200		200-250	
Mean	Max	Mean	Max	Mean	Max	Mean	Max
0.36 (0.082)	3.29 (0.75)	0.37 (0.084)	2.79 (0.64)	0.85 (0.20)	13.03 (2.98)	1.81 (0.41)	19.11 (4.38)

3.2 Impact on RT structures

The mean volume ratio between distorted RT structures and original RT structures among all patients in the study was 1.00±0.00 for CTV, PTV, femoral head left, femoral head right, bladder and rectum. For the RT structure Body it was 1.01±0.00.

The mean magnitude of the distortion in the RT structures among all patients in left-right and inferior-superior direction was 0.00±0.00 mm for CTV, PTV, femoral head left, femoral head right, bladder and rectum. For the anterior-posterior direction it was 0.01±0.00 mm. For the RT structure Body it was 0.13±0.04 mm, 0.09±0.05 mm and 0.44±0.09 mm for the left-right, anterior-posterior and inferior-superior direction.

3.3 Development of the method and dosimetric impact

A method to assess dosimetric impact of system specific distortion in an MRI only workflow was developed. The mean number of pixels in the distortion field having a negative determinant of its Jacobian among all patients were 0.008 %. The corresponding pixel positions were at the most peripheral part of the phantom data. No pixels had a determinant of its Jacobian equal to zero.

The largest mean percentage dose difference for each isodose level and the average of the median percentage dose to target and OAR (among all patients in the study) is shown in figure 3. The largest negative and positive mean percentage dose difference for all isodose levels were -0.02 %±0.13 % (isodose level bin 80 %-85 %) and 0.02 %±0.25 % (isodose level bin 5 %-10 %).

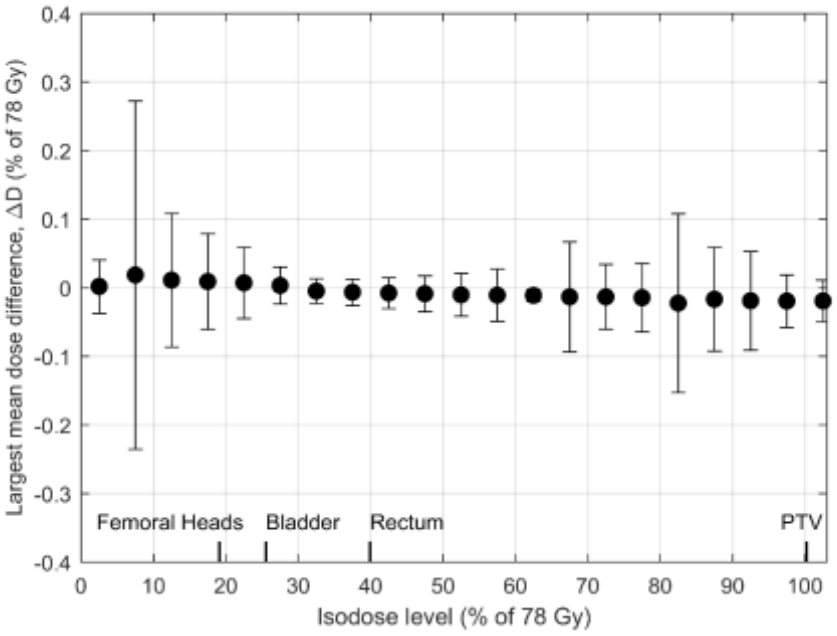

Figure 3. Largest mean percentage dose differences among all patients in the study (solid points). At each isodose level, the largest mean percentage dose difference (±1 standard deviation) among all patients in the study is shown. CT dose distribution is used as reference. The average of the median percentage dose to target and OAR among all patients in the study is shown (line markers on the isodose level axis).

4. Discussion

The work performed in this study introduced a method to assess dosimetric impact of system specific distortion in an MRI only workflow. The method was not influenced by any errors that might solely originate from the assignment of Hounsfield units in a synthetic CT generation.

The system specific distortion for an MRI only optimized sequence was assessed using a phantom. As expected, the distortion was greater with increasing radius from the isocenter of the MRI (Torfeh et al., 2015, Weygand et al., 2016). The distortion data in this study were also in good agreement with a previous study using an identical pulse sequence (Torfeh et al., 2015).

A possible interference in the measurement of the system specific distortion was object specific distortion, determined by the shape and magnetic susceptibility of the phantom material. We estimated the susceptibility effects induced by the phantom by the IDEAL IQ sequence. Using this sequence the effects from the phantom and the static magnetic field were added and could not be separated, which was an inherent limitation of the method. However, in spite of this, the measured deviations were small. Furthermore, patient specific distortions were beyond the scope of this study. The calculated mean magnitude of the object specific geometric distortion was < 0.5 mm for all radial distances of < 250 mm from the isocenter and was considered negligible for the purpose of this work. The results showed that the system specific geometric distortion were larger than the object specific geometric distortion and that non-linear gradients were the main source of the geometric distortion.

The size of the mean deviation in RT structure volume ratios were consistent with the mean magnitude of the distortion in each spatial direction for each RT structure, i.e. a larger deviation in a RT structure volume was associated with a larger distortion. This corresponded to a non-distorted anatomy of the target and OAR in the distCT images. It was previously concluded that the mean distortion for all RT structures (body excluded) for a simulated prostate MRI only treatment workflow, was < 1 mm, both with and without 3D distortion correction (Sun et al., 2015). Our results were similar.

The method developed in this work quantified the dosimetric effects from geometric distortion in MRI only treatment planning for prostate. Validation of MRI only treatment planning, using synthetically generated CTs and conventional CTs, includes several uncertainties such as repositioning between

multiple modalities, bladder- and rectum filling, and body- and organ structure changes. Additionally, the synthetic CT generation method itself can introduce an error. In previous studies specifically aimed at the assessment of dosimetric errors originating from geometric distortion of the MRI system, synthetic CTs with bulk density assignment has been used (Sun et al., 2015, Bolard and Bulling, 2016).

Earlier studies aimed to study the dose difference in generated synthetic CTs compared to conventional CTs for prostate reports a mean dose difference to target of less than 2 % (Lambert et al., 2011, Dowling et al., 2012, Kapanen et al., 2013, Korhonen et al., 2014, Siversson et al., 2015). This is higher than in the present study. This is to be expected as our method, in contrary to the studies above, focus on the uncertainties from the system specific geometric distortion and does not rely on bulk density assignment. Furthermore, dose warping (Veiga et al., 2015) has been used in our method and to the best of our knowledge, this is the first time in literature that dose warping has been used to assess the effects of distortion in an MRI only workflow.

However, in contrast to dose warping between cone beam CT and CT, our method does not rely on deformable image registration between image sets. Instead, the inverse of the measured distortion field was used. The accuracy of the approach was ensured by investigating the properties of the Jacobian. Furthermore, interpolation effects were minimized by using a high spatial resolution for all matrices (same as CT). When adopting our dose warping approach, we recommend the actions above to be performed. If the image distortion is small (i.e. central part of the images), the error introduced when simply comparing the two dose matrices without any dose warping would be small. However, this is not the case when larger image distortion exists (e.g. peripheral part of the images).

The natural body processes occurring during the MRI scan of a patient will affect the geometry of the synthetic CT. This is important to consider when evaluating the dosimetric deviations between a CT and a synthetic CT. Natural bladder filling will lead to an increase in bladder volume. A study performed, under MRI scan conditions similar to those of an MRI only prostate treatment planning session, showed an increase in bladder volume in the study subjects ranging from 3 % to 101 % (McBain et al., 2009). From our results, using an optimized acquisition protocol, it can therefore be expected that natural

bladder volume changes is significantly larger than the bladder volume changes induced by system specific geometric distortion.

For quantification of the percentage dose difference, an analysis in segmented binned isodose levels was performed. This eliminated the need for intentionally distorting the RT structures to fit the distorted anatomy of the distCT images. In previous studies this issue has been overlooked for the dosimetric evaluation by merely copying the RT structures between the MR images and CT images (Chen et al., 2004a, Chen et al., 2004b). In the present work it was shown that the influence on the RT structures due to geometric distortion from the optimized sequence were insignificant. This may not always be the case when evaluating the geometric distortion for other MRI acquisition sequences. Dose-volume histogram (DVH) analysis was therefore not included in this work as a part of the evaluation. Furthermore, in contrast to the use of DVH analysis, the segmented binned isodose levels provides information on the dose difference for a continuous range of isodose levels.

To conclude, it is of importance that the MRI acquisition sequence used for any MRI only treatment planning are validated. A method is presented in this work which may be used for this type of validation.

5. Conclusions

A method was developed to assess the dosimetric impact of system specific geometric distortion. The dosimetric impact was not influenced by any errors that could originate from the assignment of Hounsfield units in a synthetic CT generation method. It required clinical CT image material from the anatomy of interest and the production of a displacement map, originating from a measurement of a dedicated phantom designed to assess geometric accuracy in MRI. Both of these requirements should be feasible to satisfy in a clinic aiming to introduce MRI only treatment planning. The developed method enabled quantification of the dosimetric effects of MRI system specific distortion for prostate MRI only radiotherapy treatment planning. The dosimetric effect and impact on delineated RT structures were negligible. The method has the potential to be used for any MRI acquisition sequence together with any anatomy of interest.

6. Acknowledgements

This work was partially funded by Vinnova, Sweden's innovation agency, through the national project Gentle Radiotherapy with grant number 2014-00743 and “Allmänna sjukhusets i Malmö Stiftelse för bekämpande av cancer”. Ethics approval was requested for “Validering av MR som underlag för strålbehandling” and given 2015-10-19 by Regionala etikprövningsnämnden in Umeå, Avdelningen för medicinsk forskning, diary number 2015-311-31M.

7. References

ANDREASEN, D., VAN LEEMPUT, K., HANSEN, R. H., ANDERSEN, J. A. & EDMUND, J. M. 2015. Patch-based generation of a pseudo CT from conventional MRI sequences for MRI-only radiotherapy of the brain. *Med Phys,* 42**,** 1596-605.

BAKKER, C. J., MOERLAND, M. A., BHAGWANDIEN, R. & BEERSMA, R. 1992. Analysis of machine-dependent and object-induced geometric distortion in 2DFT MR imaging. *Magn Reson Imaging,* 10**,** 597-608.

BALDWIN, L. N., WACHOWICZ, K., THOMAS, S. D., RIVEST, R. & FALLONE, B. G. 2007. Characterization, prediction, and correction of geometric distortion in 3 T MR images. *Med Phys,* 34**,** 388-99.

BEIER, T. & NEELY, S. 1992. Feature-based image metamorphosis. *SIGGRAPH Comput Graph,* 26**,** 35-42.

BELLON, E. M., HAACKE, E. M., COLEMAN, P. E., SACCO, D. C., STEIGER, D. A. & GANGAROSA, R. E. 1986. MR artifacts: a review. *AJR Am J Roentgenol,* 147**,** 1271-81.

BLOMQVIST, L., BÄCK, A., CEBERG, C., ENBLADH, G., FRYKHOLM, G., JOHANSSON, M., OLSSON, L. & ZACKRISSON, B. 2013. MR in radiotherapy – an important step towards personalized treatment? Report from the SSM's scientific council on ionizing radiation within oncology. SSM.

BOLARD, G. & BULLING, S. 2016. MO-FG-CAMPUS-JeP2-03: Clinical Commissioning of MR-Only Prostate Treatment Planning Workflow. *Medical Physics,* 43**,** 3721-3721.

CHEN, L., PRICE, R. A., JR., NGUYEN, T. B., WANG, L., LI, J. S., QIN, L., DING, M., PALACIO, E., MA, C. M. & POLLACK, A. 2004a. Dosimetric evaluation of MRI-based treatment planning for prostate cancer. *Phys Med Biol,* 49**,** 5157-70.

CHEN, L., PRICE, R. A., JR., WANG, L., LI, J., QIN, L., MCNEELEY, S., MA, C. M., FREEDMAN, G. M. & POLLACK, A. 2004b. MRI-based treatment planning for radiotherapy: dosimetric verification for prostate IMRT. *Int J Radiat Oncol Biol Phys,* 60**,** 636-47.

CHEN, M., LU, W., CHEN, Q., RUCHALA, K. J. & OLIVERA, G. H. 2008. A simple fixed-point approach to invert a deformation field. *Med Phys,* 35**,** 81-8.

DEBOIS, M., OYEN, R., MAES, F., VERSWIJVEL, G., GATTI, G., BOSMANS, H., FERON, M., BELLON, E., KUTCHER, G., VAN POPPEL, H. & VANUYTSEL, L. 1999. The contribution of magnetic resonance imaging to the three-dimensional treatment planning of localized prostate cancer. *Int J Radiat Oncol Biol Phys,* 45**,** 857-65.

DORAN, S. J., CHARLES-EDWARDS, L., REINSBERG, S. A. & LEACH, M. O. 2005. A complete distortion correction for MR images: I. Gradient warp correction. *Phys Med Biol,* 50**,** 1343-61.

DOWLING, J. A., LAMBERT, J., PARKER, J., SALVADO, O., FRIPP, J., CAPP, A., WRATTEN, C., DENHAM, J. W. & GREER, P. B. 2012. An atlas-based electron density mapping method for magnetic resonance imaging (MRI)-alone treatment planning and adaptive MRI-based prostate radiation therapy. *Int J Radiat Oncol Biol Phys,* 83**,** e5-11.

EDMUND, J. M., KJER, H. M., VAN LEEMPUT, K., HANSEN, R. H., ANDERSEN, J. A. & ANDREASEN, D. 2014. A voxel-based investigation for MRI-only radiotherapy of the brain using ultra short echo times. *Phys Med Biol,* 59**,** 7501-19.

HSU, S. H., CAO, Y., HUANG, K., FENG, M. & BALTER, J. M. 2013. Investigation of a method for generating synthetic CT models from MRI scans of the head and neck for radiation therapy. *Phys Med Biol,* 58**,** 8419-35.

HUANG, K. C., CAO, Y., BAHAROM, U. & BALTER, J. M. 2016. Phantom-based characterization of distortion on a magnetic resonance imaging simulator for radiation oncology. *Phys Med Biol,* 61**,** 774-90.

JACKSON, A. S., REINSBERG, S. A., SOHAIB, S. A., CHARLES-EDWARDS, E. M., MANGAR, S. A., SOUTH, C. P., LEACH, M. O. & DEARNALEY, D. P. 2007. Distortion-corrected T2 weighted MRI: a novel approach to prostate radiotherapy planning. *Br J Radiol,* 80**,** 926-33.

JOHANSSON, A., KARLSSON, M., YU, J., ASKLUND, T. & NYHOLM, T. 2012. Voxel-wise uncertainty in CT substitute derived from MRI. *Med Phys,* 39**,** 3283-90.

KAPANEN, M., COLLAN, J., BEULE, A., SEPPALA, T., SAARILAHTI, K. & TENHUNEN, M. 2013. Commissioning of MRI-only based treatment planning procedure for external beam radiotherapy of prostate. *Magn Reson Med,* 70**,** 127-35.

KARLSSON, M., KARLSSON, M. G., NYHOLM, T., AMIES, C. & ZACKRISSON, B. 2009. Dedicated magnetic resonance imaging in the radiotherapy clinic. *Int J Radiat Oncol Biol Phys,* 74**,** 644-51.

KIM, J., GARBARINO, K., SCHULTZ, L., LEVIN, K., MOVSAS, B., SIDDIQUI, M. S., CHETTY, I. J. & GLIDE-HURST, C. 2015. Dosimetric evaluation of synthetic CT relative to bulk density assignment-based magnetic resonance-only approaches for prostate radiotherapy. *Radiat Oncol,* 10**,** 239.

KOCH, N., LIU, H. H., OLSSON, L. E. & JACKSON, E. F. 2003. Assessment of geometrical accuracy of magnetic resonance images for radiation therapy of lung cancers. *J Appl Clin Med Phys,* 4**,** 352-64.

KORHONEN, J., KAPANEN, M., KEYRILAINEN, J., SEPPALA, T. & TENHUNEN, M. 2014. A dual model HU conversion from MRI intensity values within and outside of bone segment for MRI-based radiotherapy treatment planning of prostate cancer. *Med Phys,* 41**,** 011704.

LAMBERT, J., GREER, P. B., MENK, F., PATTERSON, J., PARKER, J., DAHL, K., GUPTA, S., CAPP, A., WRATTEN, C., TANG, C., KUMAR, M., DOWLING, J., HAUVILLE, S., HUGHES, C., FISHER, K., LAU, P., DENHAM, J. W. & SALVADO, O. 2011. MRI-guided prostate radiation therapy planning: Investigation of dosimetric accuracy of MRI-based dose planning. *Radiother Oncol,* 98**,** 330-4.

MAH, D., STECKNER, M., HANLON, A., FREEDMAN, G., MILESTONE, B., MITRA, R., SHUKLA, H., MOVSAS, B., HORWITZ, E., VAISANEN, P. P. & HANKS, G. E. 2002. MRI simulation: effect of gradient distortions on three-dimensional prostate cancer plans. *Int J Radiat Oncol Biol Phys,* 53**,** 757-65.

MCBAIN, C. A., KHOO, V. S., BUCKLEY, D. L., SYKES, J. S., GREEN, M. M., COWAN, R. A., HUTCHINSON, C. E., MOORE, C. J. & PRICE, P. M. 2009. Assessment of bladder motion for clinical radiotherapy practice using cine-magnetic resonance imaging. *Int J Radiat Oncol Biol Phys,* 75**,** 664-71.

NYHOLM, T., NYBERG, M., KARLSSON, M. G. & KARLSSON, M. 2009. Systematisation of spatial uncertainties for comparison between a MR and a CT-based radiotherapy workflow for prostate treatments. *Radiat Oncol,* 4**,** 54.

PETERSCH, B., BOGNER, J., FRANSSON, A., LORANG, T. & POTTER, R. 2004. Effects of geometric distortion in 0.2T MRI on radiotherapy treatment planning of prostate cancer. *Radiother Oncol,* 71**,** 55-64.

REINSBERG, S. A., DORAN, S. J., CHARLES-EDWARDS, E. M. & LEACH, M. O. 2005. A complete distortion correction for MR images: II. Rectification of static-field inhomogeneities by similarity-based profile mapping. *Phys Med Biol,* 50**,** 2651-61.

SIVERSSON, C., NORDSTROM, F., NILSSON, T., NYHOLM, T., JONSSON, J., GUNNLAUGSSON, A. & OLSSON, L. E. 2015. Technical Note: MRI only prostate radiotherapy planning using the statistical decomposition algorithm. *Med Phys,* 42**,** 6090-7.

SUN, J., DOWLING, J., PICHLER, P., MENK, F., RIVEST-HENAULT, D., LAMBERT, J., PARKER, J., ARM, J., BEST, L., MARTIN, J., DENHAM, J. W. & GREER, P. B. 2015. MRI simulation: end-to-end testing for prostate radiation therapy using geometric pelvic MRI phantoms. *Phys Med Biol,* 60**,** 3097-109.

TADIC, T., JAFFRAY, D. A. & STANESCU, T. 2014. Harmonic analysis for the characterization and correction of geometric distortion in MRI. *Med Phys,* 41**,** 112303.

TORFEH, T., HAMMOUD, R., MCGARRY, M., AL-HAMMADI, N. & PERKINS, G. 2015. Development and validation of a novel large field of view phantom and a software module for the quality assurance of geometric distortion in magnetic resonance imaging. *Magn Reson Imaging,* 33**,** 939-49.

WALKER, A., LINEY, G., HOLLOWAY, L., DOWLING, J., RIVEST-HENAULT, D. & METCALFE, P. 2015. Continuous table acquisition MRI for radiotherapy treatment planning: distortion assessment with a new extended 3D volumetric phantom. *Med Phys,* 42**,** 1982-91.

WALKER, A., LINEY, G., METCALFE, P. & HOLLOWAY, L. 2014. MRI distortion: considerations for MRI based radiotherapy treatment planning. *Australas Phys Eng Sci Med,* 37**,** 103-13.

WANG, D., DODDRELL, D. M. & COWIN, G. 2004a. A novel phantom and method for comprehensive 3-dimensional measurement and correction of geometric distortion in magnetic resonance imaging. *Magn Reson Imaging,* 22**,** 529-42.

WANG, D., STRUGNELL, W., COWIN, G., DODDRELL, D. M. & SLAUGHTER, R. 2004b. Geometric distortion in clinical MRI systems Part I: evaluation using a 3D phantom. *Magn Reson Imaging,* 22**,** 1211-21.

VEIGA, C., LOURENCO, A. M., MOUINUDDIN, S., VAN HERK, M., MODAT, M., OURSELIN, S., ROYLE, G. & MCCLELLAND, J. R. 2015. Toward adaptive radiotherapy for head and neck patients: Uncertainties in dose warping due to the choice of deformable registration algorithm. *Med Phys,* 42**,** 760-9.

WEYGAND, J., FULLER, C. D., IBBOTT, G. S., MOHAMED, A. S., DING, Y., YANG, J., HWANG, K. P. & WANG, J. 2016. Spatial Precision in Magnetic Resonance Imaging-Guided Radiation Therapy: The Role of Geometric Distortion. *Int J Radiat Oncol Biol Phys,* 95**,** 1304-16.

WIDMARK, A. 2008. *Phase III study of HYPOfractionated RadioTherapy of intermediate risk localised Prostate Cancer* [Online]. BioMed Central. Available: http://www.isrctn.com/ISRCTN45905321 [Accessed 07/25 2016].

YOO, T. S., ACKERMAN, M. J., LORENSEN, W. E., SCHROEDER, W., CHALANA, V., AYLWARD, S., METAXAS, D. & WHITAKER, R. 2002. Engineering and algorithm design for an image processing Api: a technical report on ITK--the Insight Toolkit. *Stud Health Technol Inform,* 85**,** 586-92.